ACS APPLIED MATERIALS & INTERFACES

Research Article

Cite This: ACS Appl. Mater. Interfaces 2019, 11, 35661−35666

www.acsami.org

Two-Dimensional T-$NiSe_2$ as a Promising Anode Material for Potassium-Ion Batteries with Low Average Voltage, High Ionic Conductivity, and Superior Carrier Mobility

Yupeng Shen, Jie Liu, Xiaoyin Li, and Qian Wang*

Center for Applied Physics and Technology, Department of Materials Science and Engineering, HEDPS, BKL-MEMD, College of Engineering, Peking University, Beijing 100871, China

Supporting Information

ABSTRACT: Potassium-ion batteries (KIBs) have attracted great attention due to their unique advantages including abundant resources, low redox potential of K, and feasible usage of cheap aluminum current collector in battery assembly. In the present work, through first-principles calculations, we find that the recently synthesized two-dimensional T-$NiSe_2$ is a promising anode material of KIBs. It possesses a large capacity (247 mAh/g), small diffusion barrier (0.05 eV), and low average voltage (0.49 V), rendering T-$NiSe_2$ a high-performance KIB anode candidate. In addition, we analyze the carrier mobility of T-$NiSe_2$, and the results demonstrate that it possesses a superior carrier mobility of 1685 $cm^2/(V\,s)$, showing the potential for applications in nanoelectronic devices.

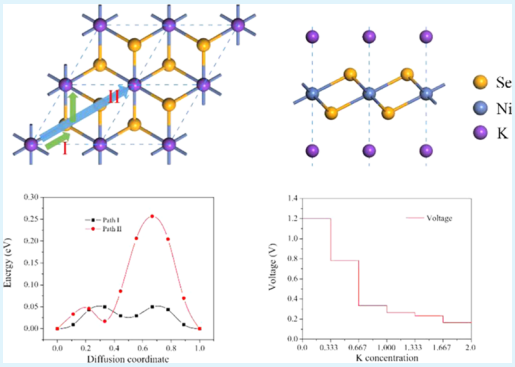

KEYWORDS: *anode, $NiSe_2$, potassium-ion battery, DFT, carrier mobility*

INTRODUCTION

With the growing requirement for power storage,[1] lithium-ion batteries (LIBs) are broadly adopted in various fields and their commercial applications have achieved great success.[2] However, the element concentration of lithium is only about 20 ppm in the earth's crust, making LIBs unsustainable in the future.[1,3,4] Hence, it is desirable to find other battery systems composed of more abundant elements. Among them, sodium-ion batteries (NIBs) and potassium-ion batteries (KIBs) are regarded as two promising candidates because of their similarity to LIBs and the abundance of Na and K (25 670 ppm for Na and 28 650 ppm for K).[5] Compared with sodium, potassium has unique advantages such as lower standard redox potential,[1] less complicated interfacial reactions[6] and higher ionic conductivity.[7,8] However, the performance of KIBs is still unsatisfying, partially attributed to the limited choices of anodes.[9]

In general, superior anode materials should possess large capacity, good cycling stability and rate capability, and low average electrode potential.[10,11] The large surface area can provide plenty of possible adsorption positions for metal atoms, resulting in high specific capacity.[12,13] Thus, anode materials with large specific surface area are favorable. Cycling stability is another key factor affecting the performance of KIB anode materials. Because of the large atomic radius of K ions, their intercalation in the conventional anode materials such as graphite usually induces large volume expansion,[9] leading to a rapid degradation in capacity and even collapse of the structure.[14] Therefore, KIB anode materials with small lattice changes during the charge/discharge process are highly desired for high-performance KIBs. In addition, the low energy barrier and short pathway of ion diffusion contribute to the high rate capability of anode materials.[15] Moreover, anodes with a low average electrode potential can provide a high output voltage when constituting full batteries. Based on the above discussions, two-dimensional (2D) materials are regarded as promising candidates for KIB anode materials because of the advantages such as high surface-to-volume ratio, small lattice changes during potassiation/depotassiation processes, and low diffusion energy barriers for K ions.[16−19]

Recently, a single-layer transition-metal diselenide, T-$NiSe_2$, was experimentally synthesized,[20] showing good promise for applications as supercapacitor,[21] hybrid supercapacitor,[22] dye-sensitized solar cell,[23] electrocatalyst,[24] and anode material for NIB.[25] However, the application of T-$NiSe_2$ as a KIB anode has not yet been reported. In this work, we first study the structural stability, electronic properties and transport properties of T-$NiSe_2$ to explore its possible application in nanoelectronic devices. Then, we investigate the performance of T-$NiSe_2$ as an anode for KIBs, including the optimal adsorption sites of K ions, capacity, diffusion barrier, open-circuit voltage, and cycling stability. The results demonstrate that T-$NiSe_2$ is a promising high-performance KIB anode candidate.

Received: May 27, 2019
Accepted: September 6, 2019
Published: September 6, 2019

DOI: 10.1021/acsami.9b09223
ACS Appl. Mater. Interfaces 2019, 11, 35661−35666

COMPUTATIONAL METHODS

Our calculations are performed based on density functional theory with the projector augmented wave method[26] by using the Vienna Ab initio Simulation Package.[27] In the calculations of structural optimization, the convergence thresholds of energy and force component are 10^{-8} eV and 10^{-6} eV/Å, respectively, and the energy cutoff is 400 eV. A vacuum space of 16 Å is placed to eliminate the influence from periodic images, and the Brillouin zone is characterized by a 17 × 17 × 1 mesh of *k*-points using the Monkhorst–Pack scheme. To take electron exchange–correlation interactions into account, Perdew–Burke–Ernzerhof (PBE) functional within generalized gradient approximation (GGA)[28] is adopted. Electronic band structure with high accuracy is calculated with Heyd–Scuseria–Ernzerhof hybrid functional.[29,30] The nudged elastic band method[31,32] is employed to evaluate the diffusion barriers of potassium ions.

RESULTS AND DISCUSSION

Geometrical Structure and Stability. There are two different phases for 2D layered $NiSe_2$, namely, the honeycomb phase (H-$NiSe_2$) and the centered honeycomb phase (T-$NiSe_2$).[33] To check the thermodynamic stability of these two structures, we calculate their structural parameters and total energies. The results are summarized in Table 1, showing good

Table 1. Calculated Lattice Constants ($a = b$), Interatomic Distances of Ni–Se (d_{Ni-Se}) and Se–Se (d_{Se-Se}), and Total Energy per $NiSe_2$ Unit Cell of T-$NiSe_2$ and H-$NiSe_2$, Respectively

	a (Å)	d_{Ni-Se} (Å)	d_{Se-Se} (Å)	total energy (eV)
T-$NiSe_2$	3.54	2.39	3.21	−13.17
H-$NiSe_2$	3.52	2.41	2.61	−12.70

consistency with previous studies.[33,34] One can see that the total energy of the T-phase is 0.47 eV/unit cell lower than that of the H-phase. Moreover, recently the T-phase $NiSe_2$ has been experimentally synthesized by Shao et al. using a single-step direct selenization method.[20] Because of the higher energetic stability and successful experimental realization, we focus on the T-phase $NiSe_2$ in the following discussions. The geometrical structure of the relaxed T-$NiSe_2$ are plotted in Figure 1a. It contains two selenium atoms and one nickel atom per unit cell and belongs to the space group of $P\bar{3}m1$ (164).

First, we examine the structural stability of the T-phase $NiSe_2$, including its dynamical, thermal, and mechanical stabilities. The phonon band structure of T-$NiSe_2$ is obtained with PHONOPY package,[35] and the results are plotted in Figure 1b. No imaginary mode can be observed in the entire Brillouin zone, confirming the dynamical stability. We then perform ab initio molecular dynamics (AIMD) simulations at 300 K for 10 000 fs by employing the Nóse heat bath scheme[36] to examine its thermal stability. To reduce the constraint resulted from the periodicity, a 4 × 4 × 1 supercell is used. As plotted in Figure 1c, the total potential energy basically remains at a fixed value and the geometric structure remains almost unchanged at the end of the molecular dynamics simulation. These results verify the thermal stability of T-$NiSe_2$ at 300 K. We further calculate the linear elastic constants by employing the energy–strain modus implemented in AELAS code[37] to analyze the mechanical stability of T-$NiSe_2$. In accordance with the Born–Huang criteria,[38] a mechanically stable 2D sheet should satisfy the relationships $C_{11}C_{22} > C_{12}^2$ and $C_{66} > 0$. Owing to the hexagonal symmetry, C_{11} is equal to C_{22}. So, in this case, the formulas become $C_{11} > |C_{12}|$ and $C_{66} >$

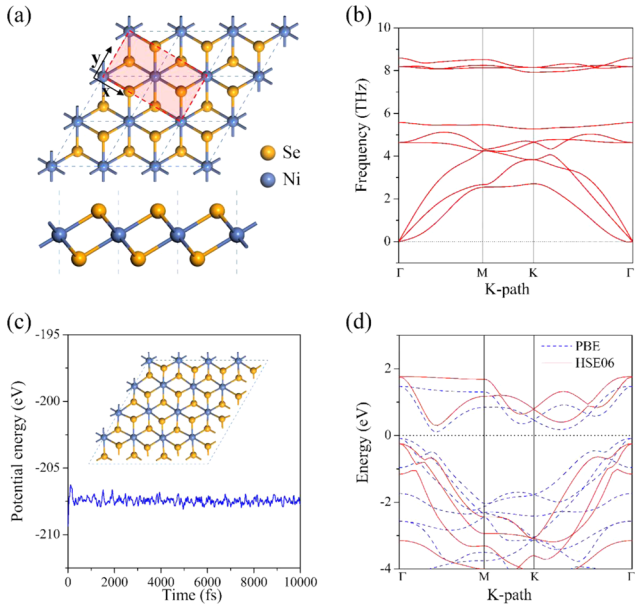

Figure 1. (a) Geometric structure of the relaxed T-$NiSe_2$ from above and from the side. The red dashed rectangle shows the orthogonal supercell of T-$NiSe_2$ (b) Phonon dispersion of the structure. (c) Energy fluctuation at 300 K during the ab initio molecular dynamics (AIMD) simulation. The top view of geometric configuration after the AIMD simulation is also plotted. (d) Electronic band structure of T-$NiSe_2$ at the GGA-PBE and HES06 levels.

0. We obtain that $C_{11} = C_{22} = 69.9$ N/m, $C_{12} = 18.8$ N/m, and $C_{66} = 25.6$ N/m, confirming the mechanical stability of T-$NiSe_2$. According to the obtained elastic constants, we calculate the Young's modulus and Poisson's ratio, which are 64.8 N/m and 0.27, respectively.

Electronic Properties. We then study the electronic properties of T-$NiSe_2$. As plotted in Figure 1d, T-$NiSe_2$ is a semiconductor with a small indirect band gap (0.19 eV at the PBE level and 0.54 eV at the HES06 level). Although a metallic anode is preferred, the material with a small band gap can also be used as an anode because it may have better electronic conductivity when metal ions are adsorbed. Many semiconducting materials with band gaps larger than that of T-$NiSe_2$ have been reported to be good anode materials, such as GeS nanosheet (1.61 eV)[10] and phosphorene (0.8 eV).[39]

To further study the transport properties of T-$NiSe_2$, we calculate its carrier mobility according to the deformation potential (DP) theory.[40] For 2D materials, the carrier mobility (μ) is estimated with the formula[41–44]

$$\mu = \frac{2e\hbar^3 C}{3k_B T|m^*|^2 E_1^2} \quad (1)$$

where T, k_B, and $\hbar$ are temperature (taken as 300 K in our calculations), Boltzmann constant, and reduced Planck constant, respectively. E_1 is the deformation potential constant and m^* is the effective mass. C is the elastic modulus calculated by $C = [\partial^2 E/\partial\delta^2]/S_0$, in which E and S_0 are the total energy and area of the supercell, respectively, and δ is the uniaxial strain. In this work, we adopt an orthogonal supercell to calculate the carrier mobility of T-$NiSe_2$ in x and y directions. Top view of the orthogonal supercell is plotted in Figure 1a in the red dashed lines. The corresponding electronic band structure of the orthogonal supercell is shown in Figure S1. It can be seen that the valence band maximum (VBM) and the

DOI: 10.1021/acsami.9b09223
ACS Appl. Mater. Interfaces 2019, 11, 35661–35666

conduction band minimum (CBM) are at the Γ point and the path of Γ−*L*, respectively.

The effective mass *m** of electrons and holes can be calculated from the equation: $m^* = \hbar^2[\partial^2 E(k)/\partial k^2]^{-1}$, in which *k* is the value of wave vector and $\hbar$ is the reduced Planck constant. The calculated results reveal that the effective masses of holes (0.86 m_e in *x* direction and 0.88 m_e in *y* direction) are about four times as large as those of electrons (0.17 m_e in *x* direction and 0.25 m_e in *y* direction). Then, the DP constants E_1 are calculated. Figure S1 displays the change of band edges (VBM and CBM) with stretching and compression (δ) in two directions. The slopes of the fitting straight lines are the corresponding DP constants, as expressed by $E_1 = dE_{edge}/d\delta$, which give similar values for holes (−4.10 eV in *x* direction and −4.02 eV in *y* direction) and electrons (−4.36 eV in *x* direction and −5.28 eV in *y* direction).

Using eq 1, the mobilities of electrons and holes at room temperature (300 K) are calculated and listed in Table 2. The

Table 2. Summarized Table of Deformation Potential Constant E_1, Elastic Modulus *C*, Effective Mass *m, and Mobility μ of T-$NiSe_2$ at 300 K**

carrier type	E_1 (eV)	*C* (N/m)	*m** (m_e)	μ ($cm^2/(V\ s)$)
electron (*x*)	−4.36	69.66	0.17	1685
electron (*y*)	−5.28	69.66	0.25	552
hole (*x*)	−4.10	69.66	0.86	78.5
hole (*y*)	−4.02	69.66	0.88	78.0

mobility of electrons is higher than that of holes in both the *x* and *y* directions, which is mainly owing to the larger effective mass of holes, thus making T-$NiSe_2$ an n-type semiconductor. It is worth noting that the carrier mobility of T-$NiSe_2$ can reach 1685 $cm^2/(V\ s)$ for electrons in the *x* direction, which is larger than that of silicene (1200 $cm^2/(V\ s)$),[45] monolayer MoS_2 (200 $cm^2/(V\ s)$),[46] and many other 2D transition metal dichalcogenide materials,[47] such as $MoSe_2$ (180 $cm^2/(V\ s)$), WS_2 (690 $cm^2/(V\ s)$), and WSe_2 (270 $cm^2/(V\ s)$), indicating the potential applications of T-$NiSe_2$ in nanoelectronics. In addition, in the *x* direction, the mobility of electrons is more than 20 times higher than that of holes, implying that the *x* direction is more conductive for electron transport. This property shows that T-$NiSe_2$ can also be used as hole/electron separation materials.

Application as an Anode Material for KIBs. Next, we explore the possibility of using T-$NiSe_2$ as an anode of KIBs. We first study the adsorption of a single K on T-$NiSe_2$. To avoid the interactions between potassium atoms, the 3 × 3 × 1 supercell is applied in the calculations. Based on the geometric symmetry of T-$NiSe_2$, we consider six different initial adsorption positions, which are plotted in Figure 2a,b. For the sake of convenience, the K atom at *x* position (*x* = 1, 2, 3, 4, 5, 6) is described as K_x. K_1 is on the top position of Ni atom, K_5 is on the top position of the upper Se atom, and K_6 is on the top position of the lower Se atom. K_2 and K_4 are, respectively, located at the bridge sites of the two Ni−Se bonds. K_3 is at the hollow site of the parallelogram consisting of Ni and Se atoms. To study the adsorption strength of K atoms on these adsorption sites, we calculate the corresponding adsorption energy (E_a) according to the following expression: $E_a = E_2 - E_1 - E_K$, where E_2 and E_1 are the total energies of the T-$NiSe_2$ with and without a K atom, respectively. E_K is the energy of a K atom in K bulk phase. After structure optimization, we find

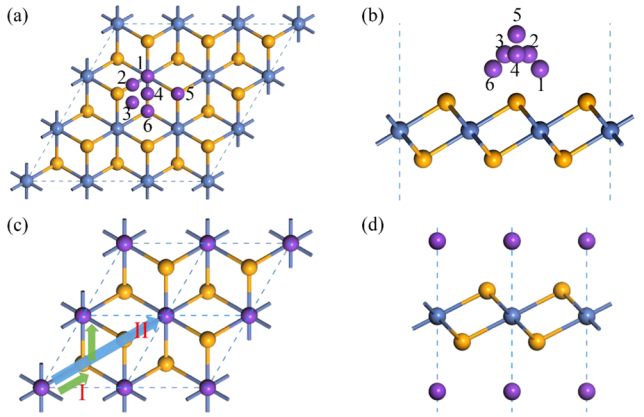

Figure 2. Geometric structure of the six possible adsorption sites (a) from above and (b) from the side. The K-saturated structure (c) from above and (d) from the side. Two calculated diffusion pathways of K ions on the T-$NiSe_2$ monolayer are also marked.

that K_1, K_4, K_5, and K_6 are stable adsorption sites, while K atoms on K_2 and K_3 sites move to K_1 and K_6 sites, respectively, after structure optimization. The corresponding adsorption energies of K on K_1, K_4, K_5, and K_6 sites are −1.44, −1.41, −1.37, and −1.13 eV, respectively, implying that K_1 is the optimal position. The results of the Bader charge analysis[48] reveal that one K atom on K_1 site transfers 0.85 electrons to T-$NiSe_2$, indicating that the K atom on K_1 donates almost all its outermost s electrons and becomes K ion. Therefore, there are strong Coulomb repulsions between these K ions, preventing them from clustering.

The electronic conductivity is critical for the performance of KIB anodes. Therefore, we calculate the band structure, total density of states (DOS) and partial density of states (PDOS) of the K adsorbed T-$NiSe_2$ sheet by using a 4 × 4 × 1 supercell. For comparison, we also calculate the total DOS and PDOS of the pristine T-$NiSe_2$ sheet. The results are plotted in Figure 3. It can be seen that T-$NiSe_2$ is semiconducting with the electronic states near the Fermi level mainly derived from the 3d electrons of Ni atoms and 4p electrons of Se atoms. After the adsorption of K atoms, the structure becomes metallic because of the shift of Fermi level, which results from the electron transfer from K atoms to the T-$NiSe_2$ sheet.

To study the migration of K ions on T-$NiSe_2$, we calculate the diffusion barriers for different paths. Considering the symmetry of the structure, two possible diffusion pathways are selected, and marked as paths I and II in Figure 2c. The energy barrier graphs of paths I and II are calculated and plotted in Figure 4a. The results demonstrate that the diffusion barriers of paths I and II are about 0.05 and 0.25 eV, respectively, indicating that K ions prefer to diffuse along path I. More importantly, the diffusion barrier of 0.05 eV is lower than that of many other 2D KIB anode materials, such as MoN_2 (0.49 eV),[18] GeSe (0.11 eV),[17] and TiS_2 (0.09 eV),[49] indicating a high ionic conductivity of T-$NiSe_2$. Besides, we also calculate the energy barrier profiles of an isolated vacancy on T-$NiSe_2$ to investigate the diffusion at high K concentration. The results, as shown in Figure S2, indicate that although the diffusion barrier (0.12 eV) is larger than that of single K-ion, it is comparable with that of GeSe (0.11 eV).[17]

We then investigate the maximum K capacity of T-$NiSe_2$ by gradually increasing the K concentration until the fully K-adsorbed configuration is obtained. The structure of the fully

DOI: 10.1021/acsami.9b09223
ACS Appl. Mater. Interfaces 2019, 11, 35661−35666

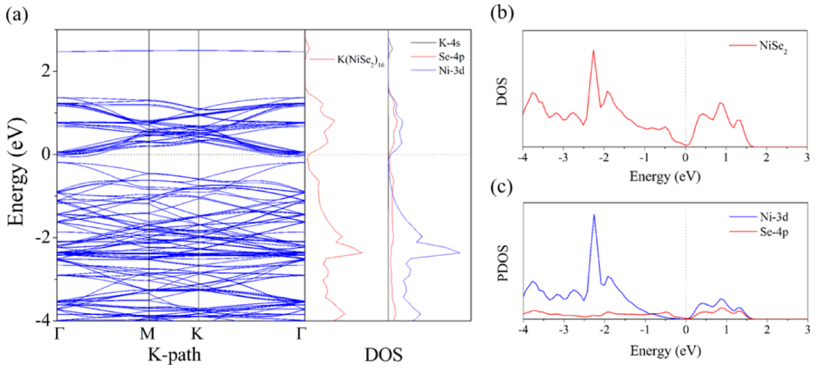

Figure 3. (a) Electronic band structure of $K(NiSe_2)_{16}$ and the corresponding total DOS and PDOS. (b) Total DOS and (c) PDOS of T-$NiSe_2$.

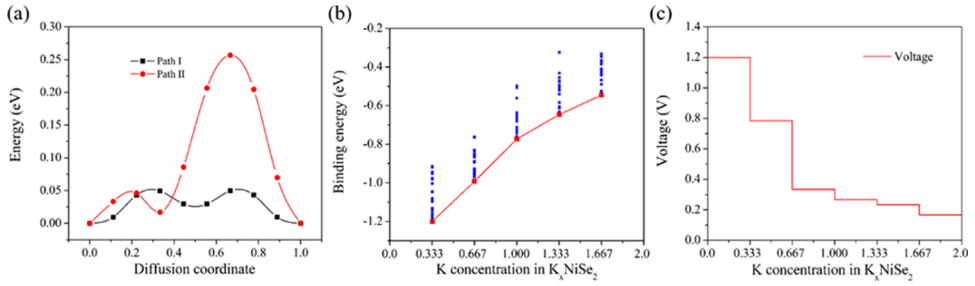

Figure 4. (a) Energy barrier graphs for diffusion paths I and II. (b) Variation of binding energy with K concentration for K_xNiSe_2 in different geometric configurations. The lowest energy for each concentration is highlighted in red. (c) Voltage−concentration relationship of T-$NiSe_2$.

K-adsorbed configuration is displayed in Figure 2c,d. Correspondingly, the theoretical capacity is 247 mAh/g (K_2NiSe_2), larger than that of many other 2D structures as anodes of KIBs, such as Nb_2C (136 mAh/g),[50] YN_2 (229 mAh/g),[51] and Ti_3C_2 (192 mAh/g),[19] making T-$NiSe_2$ an anode material with high specific capacity.

The open-circuit voltage is also a crucial indicator of anode materials. For T-$NiSe_2$, the charge/discharge process in half-cell reaction can be described as

$$(x_2 - x_1)K^+ + (x_2 - x_1)e^- + K_{x_1} - NiSe_2 \leftrightarrow K_{x_2} - NiSe_2 \quad (2)$$

Neglecting the influence of volume, entropy, and pressure, we can estimate the average voltage of K_x−$NiSe_2$ in the concentration of $x_1 < x < x_2$ by the formula

$$V \approx \frac{E_{K_{x_1}-NiSe_2} - E_{K_{x_2}-NiSe_2} + (x_2 - x_1)E_K}{x_2 - x_1} \quad (3)$$

in which $E_{K_{x1}-NiSe_2}$, $E_{K_{x2}-NiSe_2}$, and E_K are the total energy of K_{x_1}−$NiSe_2$, K_{x_2}−$NiSe_2$, and one K atom in its bulk phase, respectively. To obtain $E_{Kx-NiSe_2}$, we calculate the energies of 20 different configurations for each intermediate adsorption concentration (K_xNiSe_2: x = 0.333, 0.667, 1.000, 1.333, and 1.667) and choose the one with the lowest energy as the optimal configuration at that concentration. The calculated results are summarized in Figure 4b and the most stable configuration for each of the five different concentrations is shown in Figure S3. One can see that with increasing K concentration, the absolute value of binding energy decreases gradually because of the increase of the repulsive interactions between K ions. Then according to eq 3, we calculate and plot the corresponding voltage profile of T-$NiSe_2$, as shown in Figure 4c. During the entire adsorption process, there exist three prominent voltage platforms, separated by the two drops at the concentrations of 0.333 and 0.667, respectively. The voltage is reduced from 1.2 to 0.78 V at the concentration of 0.333; when the concentration reaches 0.667, the voltage drops to 0.33 V. After that, as the concentration increases, the voltage slowly decreases to 0.17 V. It is worth noting that the voltage remains positive in the whole process, which means that the half-cell reaction can proceed spontaneously until the final condition (K_2NiSe_2), resulting in a fully reversible capacity of 247 mAh/g. The average voltage is calculated to be 0.49 V by averaging the values across the entire area, which is in the ideal range 0.1−1.0 V for KIB anode materials[52,53] and smaller than many other 2D anode materials of KIBs such as MoN_2 (1.11 V)[18] and boron-doped graphene (0.82 V),[16] providing a higher output voltage when constituting a full battery.

We also study the cycling stability of T-$NiSe_2$ by calculating the changes of bond lengths to investigate the effect of potassiation/depotassiation process on the structure.[54,55] The degree of deformation of the structure after adsorption is a key indicator of the cycling stability because large deformation can result in loss of the capacity after cycling several times.[56] Before the adsorption of K ions, the Ni−Se bond length is 2.39 Å. At dilute (KNi_9Se_{18}) and saturated (K_2NiSe_2) concentrations, the geometric configurations remain almost intact and the Ni−Se bond lengths around the K ions are 2.40 Å (vary by 0.4%) and 2.57 Å (vary by 7.5%), respectively, implying a great cycling stability of T-$NiSe_2$.

CONCLUSIONS

In summary, by performing first-principles calculations, we have found that the T-$NiSe_2$ sheet is a promising anode material for KIBs. The advantages of T-$NiSe_2$ are reflected in the following aspects: (1) T-$NiSe_2$ possesses a small band gap

DOI: 10.1021/acsami.9b09223
ACS Appl. Mater. Interfaces 2019, 11, 35661−35666

of 0.54 eV, favoring fast kinetics of electronic transport; (2) the diffusion barrier of K atoms on T-$NiSe_2$ is 0.05 eV, indicating that K atoms can migrate fast on the structure; (3) the specific capacity (247 mAh/g) is larger than that of many other 2D anode materials for KIBs, and the system exhibits good cycling stability in the potassiation/depotassiation process; and (4) the average voltage is 0.49 V, which is in the energy range for ideal anode materials. Besides, the carrier mobility is found to be as high as 1685 $cm^2/(V\ s)$, implying the fast transport of electrons in T-$NiSe_2$. All these features suggest that T-$NiSe_2$ has great potential as an anode material of KIBs.

■ ASSOCIATED CONTENT

Supporting Information

The Supporting Information is available free of charge on the ACS Publications website at DOI: 10.1021/acsami.9b09223.

Electronic band structure of T-$NiSe_2$ in the orthogonal lattice; energy shift of the CBM and VBM with respect to the lattice stretching and compression in x and y directions, respectively; vacancy diffusion pathway on T-$NiSe_2$ and the corresponding energy barrier graph; most stable configurations of K_xNiSe_2 with x = 0.333, 0.667, 1.000, 1.333, and 1.667 (PDF)

■ AUTHOR INFORMATION

Corresponding Author

*E-mail: qianwang2@pku.edu.cn.

ORCID

Qian Wang: 0000-0002-9766-4617

Notes

The authors declare no competing financial interest.

■ ACKNOWLEDGMENTS

We acknowledge the support of the National Key Research and Development Program of China (Grant Nos. 2016YFE0127300 and 2017YFA0205003), the National Natural Science Foundation of China (NSFC-11974028 and NSFC-21773004), and the High Performance Computing Platform of Peking University, China.

■ REFERENCES

(1) Hwang, J. Y.; Myung, S. T.; Sun, Y. K. Recent Progress in Rechargeable Potassium Batteries. *Adv. Funct. Mater.* **2018**, *28*, No. 1802938.

(2) Lee, E.; Persson, K. A. Li Absorption and Intercalation in Single Layer Graphene and Few Layer Graphene by First Principles. *Nano Lett.* **2012**, *12*, 4624−4628.

(3) Ji, B.; Zhang, F.; Wu, N.; Tang, Y. A Dual-Carbon Battery Based on Potassium-Ion Electrolyte. *Adv. Energy Mater.* **2017**, *7*, No. 1700920.

(4) Xiao, W.; Wang, Z.; Zhang, Y.; Fang, R.; Yuan, Z.; Miao, C.; Yan, X.; Jiang, Y. Enhanced Performance of P(VDF-HFP)-Based Composite Polymer Electrolytes Doped with Organic-Inorganic Hybrid Particles PMMA-ZrO_2 for Lithium Ion Batteries. *J. Power Sources* **2018**, *382*, 128−134.

(5) Wedepohl, K. H. The Composition of the Continental Crust. *Geochim. Cosmochim. Acta* **1995**, *59*, 1217−1232.

(6) Moshkovich, M.; Gofer, Y.; Aurbach, D. Investigation of the Electrochemical Windows of Aprotic Alkali Metal (Li, Na, K) Salt Solutions. *J. Electrochem. Soc.* **2001**, *148*, E155−E167.

(7) Eftekhari, A.; Jian, Z.; Ji, X. Potassium Secondary Batteries. *ACS Appl. Mater. Interfaces* **2017**, *9*, 4404−4419.

(8) Glendening, E. D.; Feller, D.; Thompson, M. A. An Ab Initio Investigation of the Structure and Alkali Metal Cation Selectivity of 18-Crown-6. *J. Am. Chem. Soc.* **1994**, *116*, 10657−10669.

(9) Kim, H.; Kim, J. C.; Bianchini, M.; Seo, D. H.; Rodriguez-Garcia, J.; Ceder, G. Recent Progress and Perspective in Electrode Materials for K-Ion Batteries. *Adv. Energy Mater.* **2018**, *8*, No. 1702384.

(10) Li, F.; Qu, Y.; Zhao, M. Germanium Sulfide Nanosheet: A Universal Anode Material for Alkali Metal Ion Batteries. *J. Mater. Chem. A* **2016**, *4*, 8905−8912.

(11) Yu, H.; Cheng, X.; Xia, M.; Liu, T.; Ye, W.; Zheng, R.; Long, N.; Shui, M.; Shu, J. Pretreated Commercial $TiSe_2$ as an Insertion-Type Potassium Container for Constructing "Rocking-Chair" Type Potassium Ion Batteries. *Energy Storage Mater.* **2019**, DOI: 10.1016/j.ensm.2019.01.010.

(12) Rao, D.; Zhang, L.; Meng, Z.; Zhang, X.; Wang, Y.; Qiao, G.; Shen, X.; Xia, H.; Liu, J.; Lu, R. Ultrahigh Energy Storage and Ultrafast Ion Diffusion in Borophene-Based Anodes for Rechargeable Metal Ion Batteries. *J. Mater. Chem. A* **2017**, *5*, 2328−2338.

(13) Wang, X.; Xu, X.; Niu, C.; Meng, J.; Huang, M.; Liu, X.; Liu, Z.; Mai, L. Earth Abundant Fe/Mn-Based Layered Oxide Interconnected Nanowires for Advanced K-Ion Full Batteries. *Nano Lett.* **2017**, *17*, 544−550.

(14) Ju, Z.; Zhang, S.; Xing, Z.; Zhuang, Q.; Qiang, Y.; Qian, Y. Direct Synthesis of Few-Layer F-Doped Graphene Foam and Its Lithium/Potassium Storage Properties. *ACS Appl. Mater. Interfaces* **2016**, *8*, 20682−20690.

(15) Liu, J.; Li, X.; Wang, Q.; Kawazoe, Y.; Jena, P. A New 3D Dirac Nodal-Line Semi-Metallic Graphene Monolith for Lithium Ion Battery Anode Materials. *J. Mater. Chem. A* **2018**, *6*, 13816−13824.

(16) Gong, S.; Wang, Q. Boron-Doped Graphene as a Promising Anode Material for Potassium-Ion Batteries with a Large Capacity, High Rate Performance, and Good Cycling Stability. *J. Phys. Chem. C* **2017**, *121*, 24418−24424.

(17) Sannyal, A.; Zhang, Z.; Gao, X.; Jang, J. Two-Dimensional Sheet of Germanium Selenide as an Anode Material for Sodium and Potassium Ion Batteries: First-Principles Simulation Study. *Comput. Mater. Sci.* **2018**, *154*, 204−211.

(18) Zhang, X.; Yu, Z.; Wang, S.-S.; Guan, S.; Yang, H. Y.; Yao, Y.; Yang, S. A. Theoretical Prediction of MoN_2 Monolayer as a High Capacity Electrode Material for Metal Ion Batteries. *J. Mater. Chem. A* **2016**, *4*, 15224−15231.

(19) Er, D.; Li, J.; Naguib, M.; Gogotsi, Y.; Shenoy, V. B. Ti_3C_2 MXene as a High Capacity Electrode Material for Metal (Li, Na, K, Ca) Ion Batteries. *ACS Appl. Mater. Interfaces* **2014**, *6*, 11173−11179.

(20) Shao, Y.; Song, S.; Wu, X.; Qi, J.; Lu, H.; Liu, C.; Zhu, S.; Liu, Z.; Wang, J.; Shi, D. Epitaxial Fabrication of Two-Dimensional $NiSe_2$ on Ni (111) Substrate. *Appl. Phys. Lett.* **2017**, *111*, No. 113107.

(21) Arul, N. S.; Han, J. I. Facile Hydrothermal Synthesis of Hexapod-Like Two Dimensional Dichalcogenide $NiSe_2$ for Super-capacitor. *Mater. Lett.* **2016**, *181*, 345−349.

(22) Meng, L.; Wu, Y.; Zhang, T.; Tang, H.; Tian, Y.; Yuan, Y.; Zhang, Q.; Zeng, Y.; Lu, J. Highly Conductive $NiSe_2$ Nanostructures for All-Solid-State Battery−Supercapacitor Hybrid Devices. *J. Mater. Sci.* **2019**, *54*, 571−581.

(23) Zhang, X.; Yang, Y.; Guo, S.; Hu, F.; Liu, L. Mesoporous $Ni_{0.85}Se$ Nanospheres Grown in Situ on Graphene with High Performance in Dye-Sensitized Solar Cells. *ACS Appl. Mater. Interfaces* **2015**, *7*, 8457−8464.

(24) Mani, S.; Ramaraj, S.; Chen, S.-M.; Dinesh, B.; Chen, T.-W. Two-Dimensional Metal Chalcogenides Analogous $NiSe_2$ Nanosheets and Its Efficient Electrocatalytic Performance towards Glucose Sensing. *J. Colloid Interface Sci.* **2017**, *507*, 378−385.

(25) Zhu, S.; Li, Q.; Wei, Q.; Sun, R.; Liu, X.; An, Q.; Mai, L. $NiSe_2$ Nanooctahedra as an Anode Material for High-Rate and Long-Life Sodium-Ion Battery. *ACS Appl. Mater. Interfaces* **2017**, *9*, 311−316.

(26) Blöchl, P. E. Projector Augmented-Wave Method. *Phys. Rev. B* **1994**, *50*, 17953−17979.

(27) Kresse, G.; Furthmüller, J. Efficient Iterative Schemes for Ab Initio Total-Energy Calculations Using a Plane-Wave Basis Set. *Phys. Rev. B* **1996**, *54*, No. 11169.
(28) Perdew, J. P.; Burke, K.; Ernzerhof, M. Generalized Gradient Approximation Made Simple. *Phys. Rev. Lett.* **1996**, *77*, 3865.
(29) Heyd, J.; Scuseria, G. E.; Ernzerhof, M. Hybrid Functionals Based on a Screened Coulomb Potential. *J. Chem. Phys.* **2003**, *118*, 8207−8215.
(30) Heyd, J.; Scuseria, G. E.; Ernzerhof, M. Erratum: "Hybrid Functionals Based on a Screened Coulomb Potential" [J. Chem. Phys. 118, 8207 (2003)]. *J. Chem. Phys.* **2006**, *124*, No. 219906.
(31) Henkelman, G.; Jónsson, H. Improved Tangent Estimate in the Nudged Elastic Band Method for Finding Minimum Energy Paths and Saddle Points. *J. Chem Phys.* **2000**, *113*, 9978−9985.
(32) Henkelman, G.; Uberuaga, B. P.; Jónsson, H. A Climbing Image Nudged Elastic Band Method for Finding Saddle Points and Minimum Energy Paths. *J. Chem. Phys.* **2000**, *113*, 9901−9904.
(33) Reyes-Retana, J.; Naumis, G.; Cervantes-Sodi, F. Centered Honeycomb $NiSe_2$ Nanoribbons: Structure and Electronic Properties. *J. Phys. Chem. C* **2014**, *118*, 3295−3304.
(34) Reyes-Retana, J.; Cervantes-Sodi, F. Spin-Orbital Effects in Metal-Dichalcogenide Semiconducting Monolayers. *Sci. Rep.* **2016**, *6*, No. 24093.
(35) Togo, A.; Oba, F.; Tanaka, I. First-Principles Calculations of the Ferroelastic Transition between Rutile-Type and $CaCl_2$-Type SiO_2 at High Pressures. *Phys. Rev. B* **2008**, *78*, No. 134106.
(36) Nosé, S. A Unified Formulation of the Constant Temperature Molecular Dynamics Methods. *J. Chem. Phys.* **1984**, *81*, 511−519.
(37) Zhang, S.; Zhang, R. AELAS: Automatic Elastic Property Derivations via High-Throughput First-Principles Computation. *Comput. Phys. Commun.* **2017**, *220*, 403−416.
(38) Born, M.; Huang, K. *Dynamical Theory of Crystal Lattices*; Clarendon Press, 1954.
(39) Kulish, V. V.; Malyi, O. I.; Persson, C.; Wu, P. Phosphorene as an Anode Material for Na-Ion Batteries: a First-Principles Study. *Phys. Chem. Chem. Phys.* **2015**, *17*, 13921−13928.
(40) Bardeen, J.; Shockley, W. Deformation Potentials and Mobilities in Non-Polar Crystals. *Phys. Rev.* **1950**, *80*, 72.
(41) Dai, J.; Zeng, X. C. Titanium Trisulfide Monolayer: Theoretical Prediction of a New Direct-Gap Semiconductor with High and Anisotropic Carrier Mobility. *Angew. Chem., Int. Ed.* **2015**, *54*, 7572−7576.
(42) Jing, Y.; Ma, Y.; Li, Y.; Heine, T. GeP_3: a Small Indirect Band Gap 2D Crystal with High Carrier Mobility and Strong Interlayer Quantum Confinement. *Nano Lett.* **2017**, *17*, 1833−1838.
(43) Li, X.; Zhang, S.; Zhang, C.; Wang, Q. Stabilizing Benzene-Like Planar N_6 Rings to Form a Single Atomic Honeycomb BeN_3 Sheet with High Carrier Mobility. *Nanoscale* **2018**, *10*, 949−957.
(44) Qiao, J.; Kong, X.; Hu, Z.-X.; Yang, F.; Ji, W. High-Mobility Transport Anisotropy and Linear Dichroism in Few-Layer Black Phosphorus. *Nat. Commun.* **2014**, *5*, No. 4475.
(45) Li, X.; Mullen, J. T.; Jin, Z.; Borysenko, K. M.; Nardelli, M. B.; Kim, K. W. Intrinsic Electrical Transport Properties of Monolayer Silicene and MoS_2 from First Principles. *Phys. Rev. B* **2013**, *87*, No. 115418.
(46) Cai, Y.; Zhang, G.; Zhang, Y.-W. Polarity-Reversed Robust Carrier Mobility in Monolayer MoS_2 Nanoribbons. *J. Am. Chem. Soc.* **2014**, *136*, 6269−6275.
(47) Jin, Z.; Li, X.; Mullen, J. T.; Kim, K. W. Intrinsic Transport Properties of Electrons and Holes in Monolayer Transition-Metal Dichalcogenides. *Phys. Rev. B* **2014**, *90*, No. 045422.
(48) Tang, W.; Sanville, E.; Henkelman, G. A Grid-Based Bader Analysis Algorithm without Lattice Bias. *J. Phys.: Condens. Matter* **2009**, *21*, No. 084204.
(49) Samad, A.; Shafique, A.; Shin, Y.-H. Adsorption and Diffusion of Mono, Di, and Trivalent Ions on Two-Dimensional TiS_2. *Nanotechnology* **2017**, *28*, No. 175401.
(50) Hu, J.; Xu, B.; Ouyang, C.; Zhang, Y.; Yang, S. A. Investigations on Nb_2C Monolayer as Promising Anode Material for Li or Non-Li Ion Batteries from First-Principles Calculations. *RSC Adv.* **2016**, *6*, 27467−27474.
(51) Gong, S.; Zhang, C.; Wang, S.; Wang, Q. Ground-State Structure of YN_2 Monolayer Identified by Global Search. *J. Phys. Chem. C* **2017**, *121*, 10258−10264.
(52) Xiang, P.; Chen, X.; Xiao, B.; Wang, Z. M. Highly Flexible Hydrogen Boride Monolayer as Potassium-ion Battery Anodes for Wearable Electronics. *ACS Appl. Mater. Interfaces* **2019**, *11*, 8115−8125.
(53) Çakır, D.; Sevik, C.; Gülseren, O.; Peeters, F. M. Mo_2C as a High Capacity Anode Material: a First-Principles Study. *J. Mater. Chem. A* **2016**, *4*, 6029−6035.
(54) Sun, Q.; Dai, Y.; Ma, Y.; Jing, T.; Wei, W.; Huang, B. Ab Initio Prediction and Characterization of Mo_2C Monolayer as Anodes for Lithium-Ion and Sodium-Ion Batteries. *J. Phys. Chem. Lett.* **2016**, *7*, 937−943.
(55) Ling, C.; Mizuno, F. Boron-Doped Graphene as a Promising Anode for Na-Ion Batteries. *Phys. Chem. Chem. Phys.* **2014**, *16*, 10419−10424.
(56) Aricò, A.; Bruce, P.; Scrosati, B.; Tarascon, J.; Van Schalkwijk, W. Nanostructured Materials for Advanced Energy Conversion and Storage Devices. *Nat. Mater.* **2005**, *4*, 366−377.

DOI: 10.1021/acsami.9b09223
ACS Appl. Mater. Interfaces 2019, 11, 35661−35666